Microporous and Mesoporous Materials 326 (2021) 111350

Contents lists available at ScienceDirect

Microporous and Mesoporous Materials

journal homepage: www.elsevier.com/locate/micromeso

A robust metal-organic framework showing two distinct pores for effective separation of xenon and krypton

Li Wang [a], Jie Ding [a], Yudie Zhu [a], Zhenzhen Xu [a], Yaling Fan [a], Rajamani Krishna [b], Feng Luo [a,*]

[a] Jiangxi Key Laboratory for Mass Spectrometry and Instrumentation, School of Chemistry, Biology and Materials Science, East China University of Technology, Nanchang, 330013, PR China

[b] Van't Hoff Institute for Molecular Sciences, University of Amsterdam, Science Park 904, 1098 XH, Amsterdam, the Netherlands

ARTICLE INFO

Keywords:
MOFs
Xe/Kr separation
UNF off-gas

ABSTRACT

For Xe/Kr adsorption-based separation, the current process was focused on cryogenic distillation, which is energy intensive. Metal-organic frameworks (MOFs), as an alternative solid state adsorbents, is highly interesting. Here, we reported a new robust MOF (**ECUT-51**) with two different sizes of pores (pore A and pore B). The excellent Xe/Kr separation ability was attested by dynamic breakthrough experiments. A deep insight into the separation mechanism was further obtained via Grand Canonical Monte Carlo (GCMC) simulation and Density Functional Theory (DFT) calculation. The theoretical calculations unveiled that both Xe and Kr can be accommodated in pore A, while Kr was prohibitive in pore B.

1. Introduction

Xenon (Xe) and krypton (Kr), generated from the reprocessing of used nuclear fuels (UNF), are typical radioactive gases [1–4]. Once released into environment without being controlled, they would be seriously harmful for human body. However, since highly purified Xe and Kr have wide applications in medical imaging, lighting industry, anaesthesia and scientific research [5,6], recycling the hazardous Xe and Kr have aroused strong attention world-widely. As we know, extraction and purification of Xe and Kr from noble gases is still a huge challenge due to their chemical inertness and low concentrations (1.14 and 0.087 ppmv, respectively) in the air [7,8]. In industry, one of the typical separation strategies for the noble gases is cryogenic distillation due to the differences of the boiling points (Xe 165K and Kr 120K). However, this method is considered to be excessively energy-intensive and expensive since the cost for getting high purity Xe was high up to $5000/kg [9,10]. Therefore, development of efficient separation methods aimed to reduce the cost are urgently necessary.

As an alternative strategy, using selective solid-state adsorbents to achieve the purpose of Xe/Kr separation at ambient temperature received significant attention due to their low costs. Activated carbons and zeolites (NaA and NaX) were investigated to separate Xe and Kr [11,12]. The results showed that the adsorption of Xe by zeolites was in low capacities which limited their further applications. Recently, the application of metal-organic frameworks (MOFs), covalent-organic frameworks (COFs) and hydrogen-bonded organic frameworks (HOFs) for gas storage and separation have been widely investigated due to the advantage of mild synthetic conditions, tunable pore structure and so on [13–22]. Among these, MOFs start to emerge as a new type of solid-state adsorbents for Xe, since they possess microporous frameworks by the links of metal ions and organic ligands [23–25]. For example, Co-MOF-74 was proved to be useful for selective Xe over Kr [26]. UTSA-49 exhibits a breathing behaviour through Xe adsorption at 298 K [27]. Hao Wang et al. reported that a new MOF $Co_3(HCOO)_6$ possess high Xe/Kr selectivity (around 12) [28].

Several strategies were used to design new MOFs to improve the uptake capacity of Xe and increase the Xe/Kr selectivity. For example, theoretical studies reported that porous materials which possess a pore size around 4 Å have the best Xe adsorption and separation due to the fact that this size is similar with the kinetic diameter of Xe (4.1 Å) [29,30]. Sikora et al. also pointed out that MOFs with uniform pore sizes that just fit for single xenon atom are potential materials for adsorbents [31]. In addition, introducing polar functional groups into MOF to increase Xe/Kr selectivity also become an effective method. Several UiO-66 materials constructed by different polar ligands were synthesized and resulted in stronger interactions between Xe/Kr and framework than pristine UiO-66 [32]. SBMOF-2 was reported for selective Xe over Kr due to the existence of polar –OH groups, which provides adsorption sites for

* Corresponding author.
E-mail address: ecitluofeng@163.com (F. Luo).

https://doi.org/10.1016/j.micromeso.2021.111350
Received 8 April 2021; Received in revised form 6 August 2021; Accepted 7 August 2021
Available online 10 August 2021

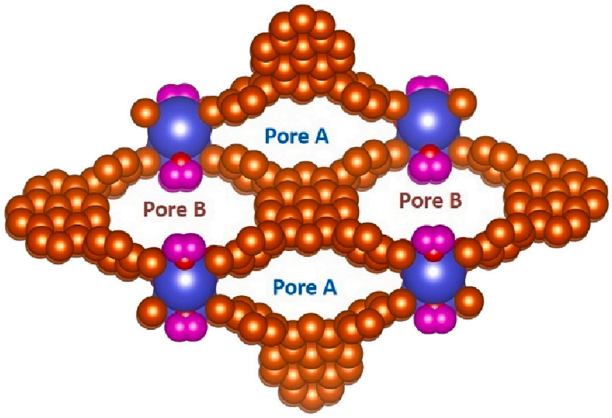

Scheme 1. The MOF including two distinct pores.

Xe [33]. Furthermore, MOFs including open metal sites also make enormous contributions to increase Xe/Kr selectivity. For example, M-MOF-74 materials (M = Co, Zn and Mg) possessing large number of unsaturated metal sites were investigated, resulting the preferential separation Xe from mixtures [26]. NKMOF-1-Ni was proved to be potential separate material for Xe/Kr mixture benefitting from open metal sites that enhance the interaction towards gas molecules [34].

However, increasing both uptake capacity and adsorption selectivity in MOFs is still a huge challenge. For example, introducing polar groups sometimes can strengthen not only Xe-framework interactions but also Kr-framework interactions, leading to lower Xe/Kr selectivity. Therefore, new type of MOFs possessing more than one pores have drawn tremendous interest for gas separation. These MOFs normally have hierarchical pores to enhance both gas uptake capacity and adsorption selectivity [35].

Targeting increasing both Xe uptake capacity and Xe/Kr selectivity, we designed a new robust 3D crystalline structure (**ECUT-51**) including two district pores (pore A and pore B) as shown in Scheme 1. 1,3,6,8-tetrakis (P-benzoic acid) pyrene (H_4TBAPy) was chosen as the ligand. As we know, the same ligand was previously used to construct several networks based on different metals such as In, Zn, Zr, and so on [36–38]. However, none of them were investigated for Xe/Kr separation. In order to explore the separation ability of **ECUT-51** from UNF off-gas, gas adsorption measurements including Xe, Kr, N_2, O_2, CO_2 were performed at different temperatures. The results demonstrated that **ECUT-51** showed a notably larger adsorption capacity for Xe than other gases. In addition, column breakthrough experiments were performed to simulate the practical application under real-world situations. As a result, **ECUT-51** showed an excellent separation ability for Xe capture. GCMC simulation based on the adsorption data proved that pore A have strong interaction between Xe and frameworks than Kr and frameworks, while pore B can only accommodate Xe (Scheme 1).

2. Experimental

Synthesis of ECUT-51 and ECUT-51a. At room temperature, the ligand H_4TBAPy (0.025 mmol, 17 mg) and Sr $(NO_3)_2$ (0.05 mmol, 11 mg) were dissolved in 3 mL N, N-dimethylformamide (DMF) and 50 μl HCl (0.6 mmol). The mixtures were sealed in a 20 mL screw-capped glass vial. The vial was heated at 110 °C for 72 h and then cooled down to 25 °C at a rate of 0.1 °C/min. The resulting yellow rod-like crystals (**ECUT-51**) were collected by filtration and washed with DMF. Bulk **ECUT-51** was synthesized using the same method and immersed into methanol for three days. The methanol was refreshed three times every day and finally the products were evacuated under dynamic vacuum at 100 °C (**ECUT-51a**). The instruments and characterization were shown in supporting information.

Gas adsorption experiments. The gas sorption isotherms were collected on a Belsorp-max. Roughly 100 mg of **ECUT-51a** were taken for the nitrogen adsorption experiments at 77 K. The adsorption isotherms for Xe/Kr were obtained at temperature of 273 K and 298 K, respectively. Liquid nitrogen and water bath were used to maintain the experimental temperatures of 77 K, 273 K, and 298 K. The isosteric heats of adsorption (Q_{st}) were calculated based on Clausius-Clapeyron equation. The adsorption selectivity was established by the Ideal Adsorbed Solution Theory (IAST) for Xe/Kr (20:80), Xe/CO_2 (1:99), Xe/O_2 (1:99),

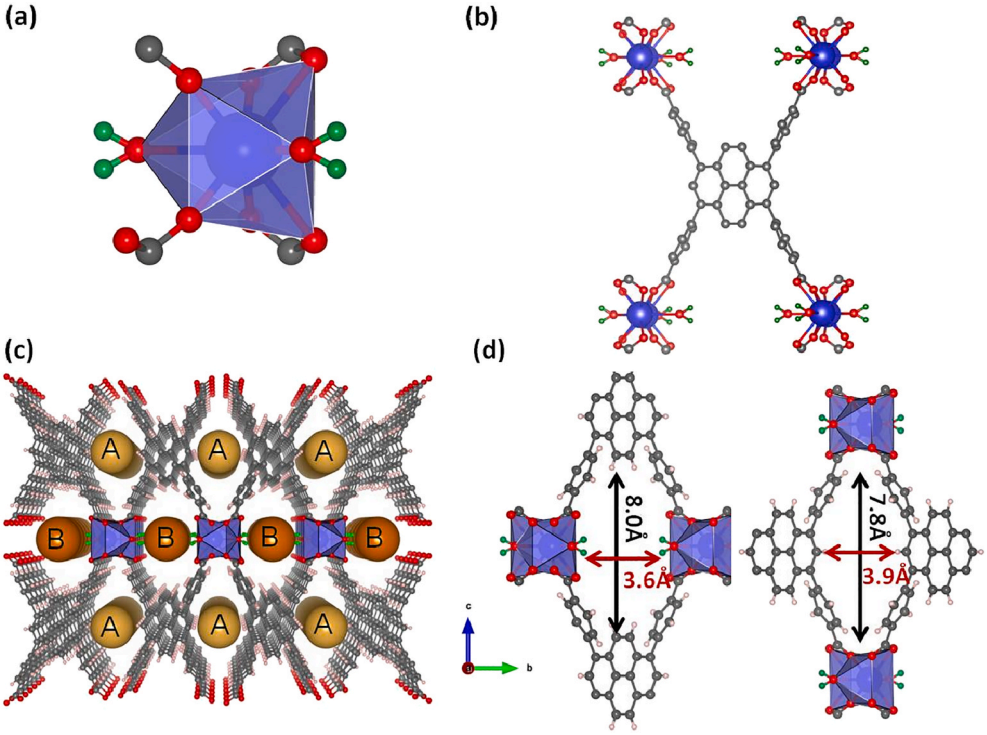

Fig. 1. Structure of **ECUT-51**: (a) The coordination environment of the metal Sr. (b) the coordination environment of TBAPy ligands. (c) Three-dimensional view of **ECUT-51**. The colored spheres represent two different pores (pore A and pore B). (d) The apertures of different pores. The polyhedral coordination around Sr was denoted as purple, oxygen in red, carbon in grey, hydrogen in pink and only hydrogen from water molecules in green. (For interpretation of the references to color in this figure legend, the reader is referred to the Web version of this article.)

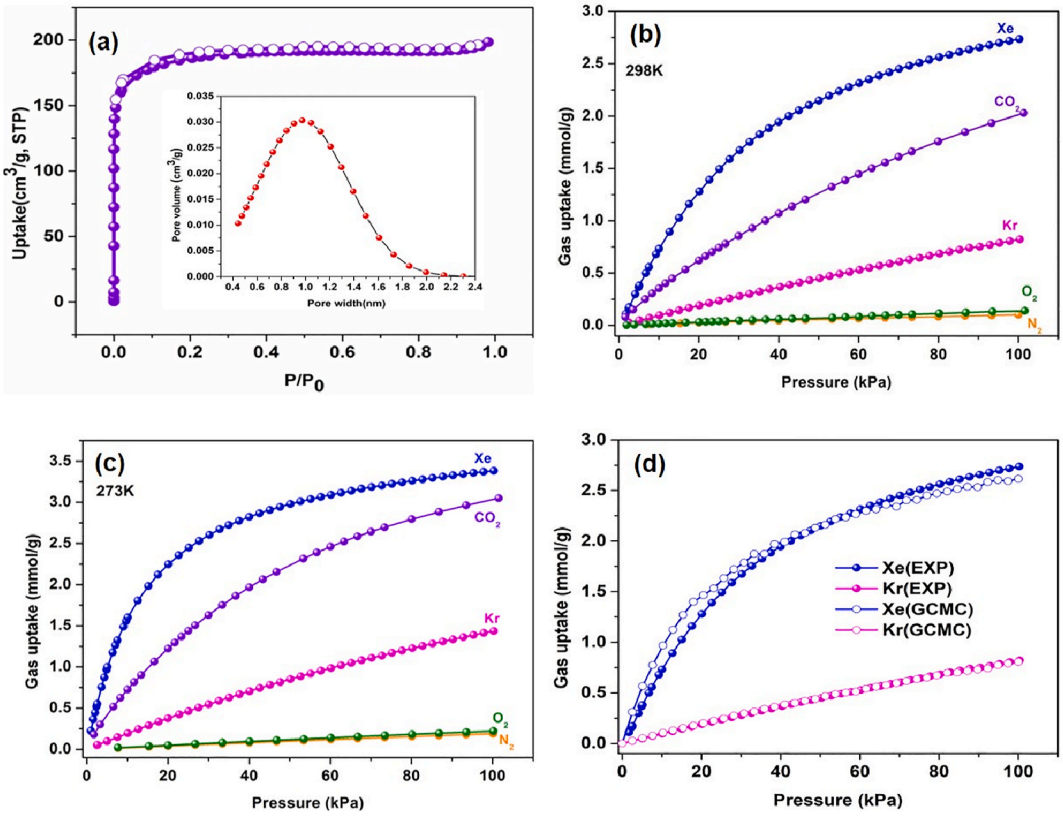

Fig. 2. The adsorption and separation data of ECUT-51. (a) The N_2 adsorption and desorption isotherms at 77 K with the inset of the distribution of pore seize. (b) and (c) Experimental single-component adsorption isotherms of different gases at 298 K and 273 K, respectively. (d) The adsorption isotherms of Xe and Kr at 298 K, including experiments and simulations.

and Xe/N_2 (1:99) mixtures at 298 K.

Breakthrough experiments. The breakthrough experiments were performed at 298 K. Bulk **ECUT-51a** (around 1.3g) were filled into stainless steel column. First, the helium gas (100 mL/min) was introduced into the column for 30 min. Then the Xe/Kr mixture (20/80) or simulated UNF off-gas (400 ppm Xe, 40 ppm Kr, 78.1% N_2, 20.9% O_2, 0.03% CO_2 and 0.9% Ar) passed through the column with 2 mL/min. The eluted gas stream from the column is monitored by a gas chromatography (TCD-Thermal Conductivity Detector, detection limit 0.1%). Prior to each cycling experiment, the adsorption bed was regenerated by He flow for 3h at 333K to ensure complete removal of adsorbed gas.

3. Results and discussion

3.1. Material synthesis and characterization

The single crystal structure of **ECUT-51** revealed that it crystallized in the orthorhombic space group *Pbam*. The detailed information for this single crystal was shown in Table S1 and Table S2. Crystallographic data for **ECUT-51** have been deposited (CCDC 1974917).

The coordination environment of **ECUT-51** for the metal and ligands are shown in Fig. 1. Only one crystallographic site was found for Sr1. The Sr1 was coordinated with six carboxylated-O from four TBAPy ligands and two water molecules, exhibiting distorted polyhedron with the Sr–O bond lengths between 2.47 Å and 2.73 Å. Adjacent Sr atoms were connected by oxygen from coordinated water molecules and TBAPy ligands, generating an infinite 1 D metal chain parallel to the crystallographic *a* axis. Each TBAPy ligand includes four benzoate groups which were appended at 1-,3-,6- and 8- positions of the pyrene core and was coordinated with Sr atom as shown in Fig. 1b. Two diamond-shaped channels with the size of 7.8 × 3.9 Å (pore A) and 8.0 × 3.6 Å (pore B, considering the van der Waals radii of atoms) along the crystallographic *a* axis were formed in **ECUT-51** (Fig. 1c and d). It should be noticed that the size of pore A were comparable with the diameter of Xe (4.1 Å) atom and slightly bigger than that of Kr (3.655 Å), suggesting that this pore might adsorb both Xe and Kr. As for pore B, which had a pore-limiting diameter of 3.6 Å, this size seemed too narrow to accommodate both Xe and Kr. However, the polarizability of Xe was notably higher than Kr, which is also an important factor for affecting the adsorption behaviour [38–40]. As a result, Xe could be efficiently adsorbed by pore B due to its high polarizability. This was also further confirmed by theoretical calculation afterwards.

For further investigation, bulk materials were synthesized using solvothermal method. PXRD patterns for the bulk materials of **ECUT-51** and simulated curves from single crystal data were shown in Fig. S1. No other extra peak was found in the bulk materials, confirming the phase purity.

3.2. Thermalgravimetric analysis

To examine the thermal stability of **ECUT-51**, TG curves were obtained between room temperature and 800 °C under N_2 atmosphere (Fig. S2). It can be seen that a slight weight loss occurred in the range of 25 °C–100 °C. This was corresponded to the loss of guest solvent molecules. **ECUT-51** remained stable up to approximately 530 °C. Above 530 °C, more than 30% weight loss was observed, indicating decomposition of the skeleton structure of **ECUT-51**. From Fig. S2, it can be speculated that the evacuation temperature of **ECUT-51** for removing the solvent guests was as high as 350 °C. Fortunately, the guests can be replaced by methanol. After being soaked in methanol, the evacuation temperature of **ECUT-51** can be decreased to a much lower temperature (200 °C under vacuum) to obtain the activated samples **ECUT-51a** (Fig. S2). The similar PXRD patterns of **ECUT-51** after immersion in methanol and activated **ECUT-51** indicated that the framework was well

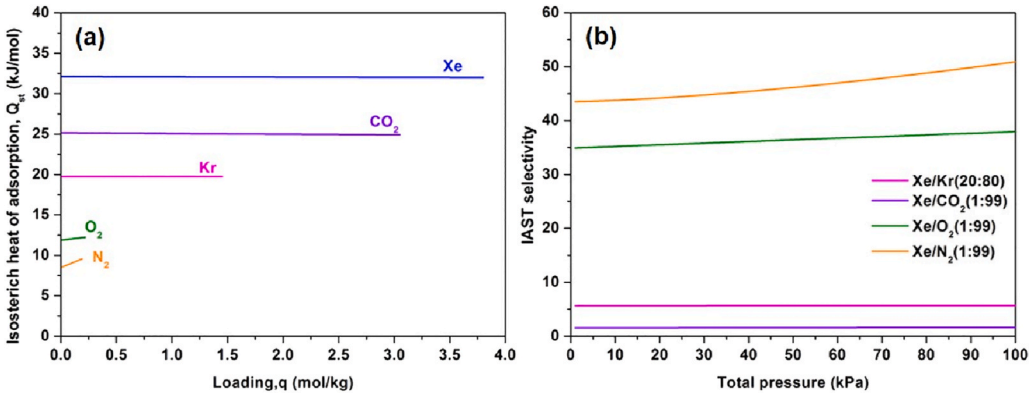

Fig. 3. (a) The isosteric heats adsorption (Q_{st}) for different gases. (b) IAST selectivity data for different gases.

maintained (Fig. S1).

3.3. Porosity measurement

Inspired by the crystal structure, the porosity of **ECUT-51a** was explored through N_2 adsorption (Fig. 2a). The resulted adsorption and desorption isotherms for **ECUT-51a** exhibited a typical reversible behaviour. Obviously, at relatively low pressures, **ECUT-51a** reached an uptake capacity around 195 cm^3/g. As the pressure increased, the uptake capacity maintained constantly, exhibiting a typical type-I isotherm and presenting the microporous nature. The BET surface area of **ECUT-51a** was calculated to be 708 m^2/g.

3.4. Gas adsorption

The permanent porosity of **ECUT-51a**, as well as the intriguing structure with two district pores, encouraged us to examine its performance for gas adsorption and separation. Different single-component gases such as Xe, Kr, CO_2, O_2, N_2 were chosen to measure the adsorption and desorption isotherms of **ECUT-51a**. Fig. 2b and c exhibited the adsorption isotherms of Xe, Kr, CO_2, O_2, N_2 at different temperatures for **ECUT-51a**. A typical type I behaviour was shown in the isotherms of Xe at either 298 K or 273 K. At 298 K, the maximum uptake capacity of Xe, Kr, CO_2, O_2, and N_2 reached to 2.7, 0.8, 2.0, 0.14, and 0.1 mmol/g, respectively. At 273 K, the corresponding uptake capacity were elevated to 3.4, 1.4, 3.05, 0.22, and 0.19 mmol/g, respectively. The maximal adsorption capacity for these gases decreased from 273 K to 298 K, indicating the property of physical adsorption. The uptake capacity of Xe was larger than Kr. The possible reason was that Xe have higher polarizability than Kr, leading to a stronger affinity between Xe and the MOF. At 298 K and 1 atm, it should be noticed that the Xe/Kr uptake ratio was up to 3.4-fold, which was comparable with other reported MOFs (Fig. S3) [39,41–43]. To our knowledge, only scarce reported MOFs displayed an outstanding performance on both adsorption capacity and uptake ratio. For example, the Xe uptake of HKUST-1 reached to 3.3 mmol/g, however the Xe/Kr uptake ratio was much lower than our MOF. Co-MOF-74 possessed high Xe uptake capacity (~6.7 mmol/g), but the uptake ratio is 3.6, which was similar to ours. In comparison, our MOF displayed a balanced performance on either Xe capacity or Xe/Kr uptake ratio due to the unique structure of pore A and pore B.

The Q_{st} of Xe, Kr, CO_2, O_2, N_2 on **ECUT-51a** were calculated based on experimental adsorption isotherms (Fig. 3a). The Q_{st} of Xe was calculated to be 32 kJ/mol, higher than that of Kr (21 kJ/mol), CO_2 (25.2 kJ/mol), O_2 (11.89 kJ/mol), N_2 (8.55 kJ/mol), indicating the higher selectivity of **ECUT-51** towards Xe atoms. As far as we know, the Q_{st} value of Xe was lower than other materials such as squarate-based MOF (43.6 kJ/mol) [39], CROFOUR-1-Ni (37.4 kJ/mol) [41], and SBMOF-1 (35 kJ/mol) [24], but it was significantly higher than MOF-5 (15 kJ/mol) [19], $Co_3(HCOO)_6$ (29 kJ/mol) [28], and CROFOUR-2-Ni (30.5 kJ/mol) [41], indicating that the suitable pore size was one of the important factors for improving the adsorption efficiency of Xe.

Furthermore, the selectivity of Xe/other gases were calculated by the ideal adsorbed solution theory (IAST). The adsorption selectivity of Xe with respect to Kr was 5.6 at 100 kPa (Fig. 3b). This value was lower than other representative MOFs such as SB-MOF-1 (~16) [24], MOF-Cu-H(~16.7) [1], squarate-based MOF(~69.7) [39], but it was in the medium level among the MOFs such as NU-403(~2) [44] and Ni-MOF-74 (~6) [23]. The selectivity for Xe/CO_2, Xe/O_2, and Xe/N_2 were estimated to be around 2.0, 34, and 43, respectively, based on the concentration of 1% Xe. In this regard, it can be predicted that separation of Xe from UNF off-gas was possible for **ECUT-51**. Additionally, Henry's coefficient was a useful measure to evaluate the affinity

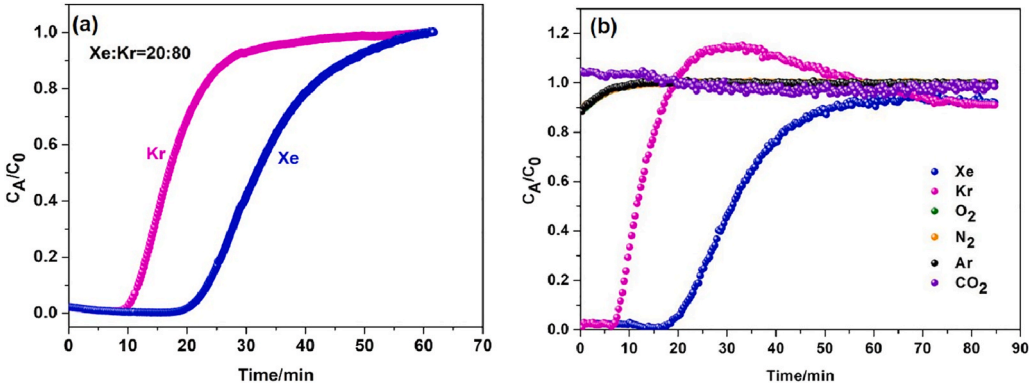

Fig. 4. Single column breakthrough experiments using **ECUT-51a** at 298K and 1 bar. (a) The gas mixture was Xe/Kr = 20:80. (b) The gas mixture was 400 ppm Xe, 40 ppm Kr, 78.1% N_2, 20.9% O_2, 0.03% CO_2 and 0.9% Ar. The breakthrough curves of N_2 and O_2 overlapped and they are covered by Ar.

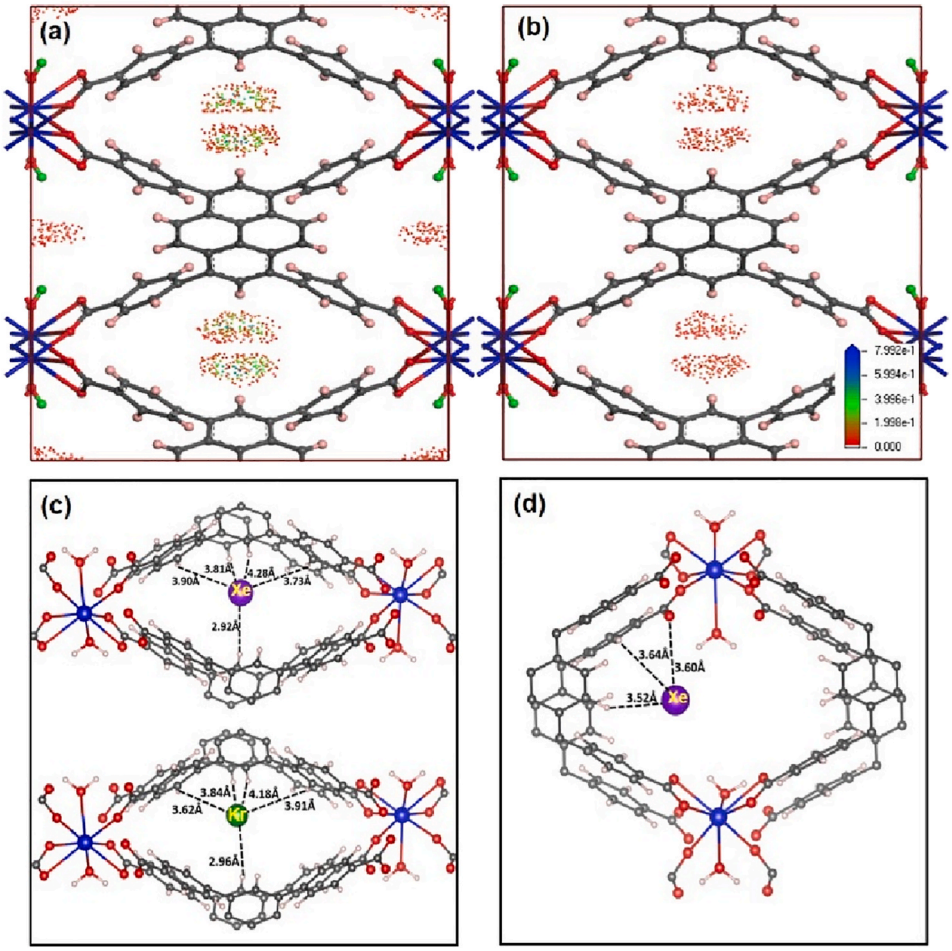

Fig. 5. Density distribution of Xe (a) and Kr (b) molecules in **ECUT-51a** at 298 K and 100 kPa. (c) The interactions between Xe/Kr and **ECUT-51a** in pore A. (d)The interactions between Xe and **ECUT-51a** in pore B. Color code: C/grey, O/red, Sr/blue, H/pink, Xe/purple, Kr/green. (For interpretation of the references to color in this figure legend, the reader is referred to the Web version of this article.)

between adsorbents and adsorbates at low pressures. The Henry coefficients were calculated from single-component Xe and Kr adsorption isotherms at 298 K (Fig. S4 and S5). It can be seen that **ECUT-51** exhibited the Henry coefficient value of 8.22 mmol/g/bar for Xe and Xe/Kr Henry's selectivity of 8.70. These values are comparable to other reported MOFs such as Ni-MOF-74 (8.40 mmol/g/bar and 5.8), SB-MOF-2 (10.45 mmol/g/bar and 8.6), $[Co_3(HCOO)_6]$ (9.93 mmol/g/bar and 8.7) and MOF-505 (10.26 mmol/g/bar and 6.8).

3.5. Single column breakthrough experiments

To check the separation ability of **ECUT-51a** in real world, single column breakthrough experiment with Xe/Kr mixture (20:80) was carried out. After being initially purged with He, the mixed gas passed through the column (12 mm in diameter) packed with **ECUT-51a** with the flow rate of 2 mL/min. It can be seen that Kr eluted out of the column after 10 min, while Xe was remained strongly inside the column and was detected after 20 min (Fig. 4a). Under this condition, the adsorption capacity of Xe was calculated to be 0.47 mmol/g, which matched well with the adsorption capacity (0.50 mmol/g) at 0.06 bar. The result suggested that **ECUT-51a** displayed a preferential adsorption and selectivity towards Xe over Kr. Furthermore, cycling experiments on **ECUT-51** were carried out under the same condition to check the regenerability (Fig. S6). Through another two-time cycling experiments, the breakthrough time interval for Xe and Kr remained almost identical, indicating the excellent regenerability of **ECUT-51**.

In addition, breakthrough experiment with simulated UNF off-gas was also carried out to examine the separation ability of **ECUT-51a** with Xe and Kr at lower concentration. As shown in Fig. 4b, CO_2, N_2, O_2, and Ar eluted firstly from the column. After about 6 min, Kr broke through the column, while Xe was not detectable until around 18 min. This result strongly suggested that **ECUT-51** can effectively separate Xe from UNF off-gas.

3.6. Theoretical calculation

To further figure out the adsorption and separation behaviour of **ECUT-51**, GCMC simulations were employed to elucidate the nature binding sites of these gases in **ECUT-51a** at molecular level. Since the uptake capacity of N_2 and O_2 are quite low, their simulations were not discussed in this work. The simulated and experimental isotherms for Xe, Kr, and CO_2 were compared in Fig. 2d and Fig. S7. Regardless of the adsorption trend or the adsorption capacity, only negligible discrepancies could be found between simulated and experimental isotherms.

The density distribution of Xe, Kr, and CO_2 molecules in the structure of **ECUT-51a** at 298 K were further studied. From Fig. 5 and Fig. S8, it can be seen that Xe and CO_2 could fill in both pore A and pore B, while Kr was preferentially loaded in pore A. This result was in agreement with that of the single-component adsorption experiment which also showed that Xe and CO_2 had higher uptake capacity than Kr. In other words, pore A contributed to the high adsorption capacity due to its tolerance to all the gases. In comparison, Kr was prevented to be adsorbed in pore B. The different binding sites for Xe and Kr may explain the resulted selectivity for **ECUT-51a**. The calculated binding energies of Xe was

−36.14 kJ/mol (in pore A) and −34.14 kJ/mol (in pore B), far exceeding the corresponding Kr value (−24.66 kJ/mol in pore A), indicating the strong Xe-framework interactions.

As shown in Fig. 5c, the distance between Xe and H atoms (2.92 Å) which was from phenyl ring, was significantly shorter than the average distance between Xe and H atoms (3.71 Å) [9], indicating that Xe atoms have strong network-gas interactions. In other words, Xe atoms can be trapped firmly in pore A. The distance between Kr and H atoms was 2.96 Å. In pore B, the calculated distance (3.52 Å) between Xe and H was longer than that in pore A, indicating weaker interactions between Xe and pore B. In addition, the Xe···O (from the ligand) distance was 3.60 Å, which was shorter than the reported distances (3.86 Å and 4.26 Å) [9]. On the contrary, no appropriate adsorption sites were found for Kr in pore B from the calculation. Based on the above results, we can conclude that pore A can effectively promote the Xe uptake, while pore B can only accommodate Xe atom, which resulted in the desired separation.

4. Conclusions

In summary, a new 3-D MOF (**ECUT-51**) with two different pores has been designed. One pore can be filled with both Xe and Kr, while another pore can only accommodate Xe. Dynamic breakthrough experiments at room temperature further confirmed that **ECUT-51** can effectively separate Xe and Kr. In addition, separation of trace Xe/Kr from a simulated UNF off-gas was also explored and the separation ability of **ECUT-51** was further verified. In all, the preferred adsorption of Xe over Kr in **ECUT-51** could be ascribed to the suitable pore size and high polarizability of Xe.

CRediT authorship contribution statement

Li Wang: Conceptualization, Writing – original draft. **Jie Ding:** Investigation. **Yudie Zhu:** Investigation. **Zhenzhen Xu:** Software, Validation. **Yaling Fan:** Resources. **Rajamani Krishna:** Formal analysis. **Feng Luo:** Supervision, Writing – review & editing.

Declaration of competing interest

The authors declare that they have no known competing financial interests or personal relationships that could have appeared to influence the work reported in this paper.

Acknowledgment

We thanks to the Open Fund of Jiangxi Key Laboratory for Mass Spectrometry and Instrumentation (JXMS202007), the Doctoral Scientific Research Start-up Foundation of East China University of Technology (DHBK2018044), and the National Natural Science Foundations of China (21966002, 21871047).

Appendix A. Supplementary data

Supplementary data to this article can be found online at https://doi.org/10.1016/j.micromeso.2021.111350.

References

[1] S. Xiong, Y. Gong, S. Hu, X. Wu, W. Li, Y. He, B. Chen, X. Wang, A microporous metal-organic framework with commensurate adsorption and highly selective separation of xenon, J. Mater. Chem. A. 6 (2018) 4752–4758.
[2] D. Banerjee, A.J. Cairns, J. Liu, R.K. Motkuri, S.K. Nune, C.A. Fernandez, R. Krishna, D.M. Strachan, P.K. Thallapally, Potential of metal-organic frameworks for separation of xenon and krypton, Accounts Chem. Res. 48 (2015) 211–219.
[3] D. Banerjee, C.M. Simon, S.K. Elsaidi, M. Haranczyk, P.K. Thallapally, Xenon gas separation and storage using metal-organic frameworks, Inside Chem. 4 (2018) 466–494.
[4] N.R. Soelberg, T.G. Garn, M.R. Greenhalgh, J.D. Law, R. Jubin, D.M. Strachan, P. K. Thallapally, Radioactive iodine and krypton control for nuclear fuel reprocessing facilities, Science and Technology of Nuclear Installations (2013) 1–12, 2013.
[5] L.T. Liu, Y. Xu, P. Tang, Mechanistic insights into xenon inhibition of NMDA receptors from MD simulations, J. Phys. Chem. B 114 (2010) 9010–9016.
[6] G.A. Lane, M.L. Nahrwold, A.R. Tait, M. Taylor-Busch, P.J. Cohen, A.R. Beaudoin, Anesthetics as teratogens:nitrous oxide is fetotoxic, xenon is not, Science 210 (1980) 899–901.
[7] G. Yu, Y. Liu, X. Zou, N. Zhao, H. Rong, G. Zhu, A nanosized metal–organic framework with small pores for kinetic xenon separation, J. Mater. Chem. A. 6 (2018) 11797–11803.
[8] B. Liu, Y. Gong, X. Wu, Q. Liu, W. Li, S. Xiong, S. Hu, X. Wang, Enhanced xenon adsorption and separation with an anionic indium–organic framework exchange with Co^{2+}, RSC Adv. 7 (2017) 55012–55019.
[9] L. Chen, P. Reiss, S.Y. Chong, D. Holden, K.E. Jelfs, T. Haswell, M.A. Little, A. Kewley, M.E. Briggs, A. Stephenson, K.M. Thomas, J.A. Armstrong, J. Bell, J. Busto, R. Noel, J. Liu, D.M. Strachan, P.K. Thallapally, A.I. Copper, Separation of rare gases and chiral molecules by selective binding in porous organic cages, Nat. Mater. 13 (2014) 954–960.
[10] S. Elsaidi, D. Ongari, W. Xu, M. Monhamed, M. Haranczyk, P. Thallapally, Xenon recovery at room temperature using metal–organic frameworks, Chemistry-A European Journal 23 (2017) 10758–10762.
[11] C.G. Saxton, A. Kruth, M. Castro, P.A. Wright, R.F. Howe, Xenon adsorption in synthetic chabazite zeolites, Microporous Mesoporous Mater. 129 (2010) 68–73.
[12] T.A. Kuznetsova, A.M. Tolmachev, N.G. Kryuchenkova, D.A. Firsov, A.A. Fomkin, Thermodynamics of adsorption of krypton, xenon, nitrogen, and oxygen on microporous active carbon at temperatures above critical values, Prot Met Phys Chem Surf 49 (2013) 367–372.
[13] J.D. Pang, S. Yuan, J.S. Qin, C.T. Lollar, N. Huang, J.L. Li, Q. Wang, M.Y. Wu, D. Q. Yuan, M.C. Hong, H.C. Zhou, Tuning the ionicity of stable metal–organic frameworks through ionic linker installation, J. Am. Chem. Soc. 141 (2019) 3129–3236.
[14] S.L. Hou, J. Dong, X.L. Jiang, Z.H. Jiao, B.A. Zhao, Noble-metal-free metal–organic framework (MOF) catalyst for the highly efficient conversion of CO2 with propargylic Alcohols, Angew. Chem. Int. Ed. 58 (2019) 577–581.
[15] F. Yang, G. Xu, Y.B. Dou, B. Wang, H. Zhang, H. Wu, W. Zhou, J.R. Li, B.L. Chen, A flexible metal–organic framework with a high density of sulfonic acid sites for proton conduction, Nat. Energy. 2 (2017) 877–883.
[16] Y.B. Zhang, L.F. Yang, L.Y. Wang, S. Duttwyler, H. B Xing, Assembled from a Cu II dodecaborate cluster complex for selective gas separation, Angew. Chem. Int. Ed. 58 (2019) 8145–8150.
[17] Y.L. Peng, C.H. He, T. Pham, T. Wang, P.F. Li, R. Krishna, K.A. Forrest, A. Hogan, S. Suepaul, B. Space, M. Fang, Y. Chen, M.J. Zaworotko, J.P. Li, L.B. Li, Z.J. Zhang, P. Cheng, B.L. Chen, Robust microporous metal–organic frameworks for highly efficient and simultaneous removal of propyne and propadiene from propylene, Angew. Chem. Int. Ed. 58 (2019) 10209–10214.
[18] L. Wang, L. Yang, L. Gong, R. Krishna, Z. Gao, Y. Tao, W. Yin, Z. Xu, F. Luo, Constructing redox-active microporous hydrogen-bonded organic framework by imide-functionalization: photochromism, electrochromism, and selective adsorption of C2H2 over CO2, Chem. Eng. J. 383 (2020) 123117.
[19] P.K. Thallapally, J.W. Grate, R.K. Motkuri, Facile xenon capture and release at room temperature using a metal–organic framework: a comparison with activated charcoal, Chem. Commun. 48 (2012) 347–349.
[20] C.A. Fernandez, J. Liu, P.K. Thallapally, D.M. Strachan, Switching Kr/Xe selectivity with temperature in a metal–organic framework, J. Am. Chem. Soc. 134 (2012) 9046–9049.
[21] A.S. Dorcheh, D. Denysenko, D. Volkmer, W. Donner, M. Hirscher, Noble gases and microporous frameworks; from interaction to application, Microporous Mesoporous Mater. 162 (2012) 64–68.
[22] F. Luo, C. Yan, L. Dang, R. Krishna, W. Zhou, H. Wu, X. Dong, Y. Han, T. Hu, M. O'Keeffe, L. Wang, M. Luo, R. Lin, UTSA-74: a MOF-74 isomer with two accessible binding sites per metal center for highly selective gas separation, J. Am. Chem. Soc. 138 (2016) 5678–5684.
[23] J. Liu, P.K. Thallapally, D. Steachan, Metal–Organic frameworks for removal of Xe and Kr from nuclear fuel reprocessing plants, Langmuir 28 (2012) 11584–11589.
[24] D. Banerjee, C.M. Simon, A.M. Plonka, R.K. Motkuri, J. Liu, X. Chen, B. Amit, J. B. Parise, M. Haranczyk, P.K. Thallapally, Metal–organic framework with optimally selective xenon adsorption and separation, Nat. Commun. 7 (2016) ncomms11831.
[25] S.J. Lee, T.U. Yoon, A.R. Kim, S.Y. Kim, K.H. Cho, Adsorptive separation of xenon/krypton mixtures using a zirconium-based metal-organic framework with high hydrothermal and radioactive stabilities, J. Hazard Mater. 320 (2016) 513–520.
[26] S.J. Lee, K.C. Kim, T.U. Yoon, M.B. Kim, Y.S. Bae, Selective dynamic separation of Xe and Kr in Co-MOF-74 through strong binding strength between Xe atom and unsaturated Co^{2+}site, Microporous Mesoporous Mater. 236 (2016) 284–291.
[27] S. Xiong, Q. Liu, Q. Wang, W. Li, Y. Tang, X. Wang, S. Hu, B. Chen, A flexible zinc tetrazolate framework exhibiting breathing behaviour on xenon adsorption and selective adsorption of xenon over other noble gases, J. Mater. Chem. A. 3 (2015) 10747–10752.
[28] H. Wang, K. Yao, Z. Zhang, J. Jagiello, Q. Gong, Y. Han, J. Li, The first example of commensurate adsorption of atomic gas in a MOF and effective separation of xenon from other noble gases, Chem. Sci. 5 (2014) 620–624.
[29] P. Ryan, O.K. Farha, L.J. Broadbelt, R.Q. Snurr, Computational screening of metal-organic frameworks for xenon/krypton separation, AIChE J. 57 (2010) 1759–1766.

[30] C.M. Simon, R. Mercado, S.K. Schnell, B. Smit, M. Haranczyk, What are the best materials to separate a xenon/krypton mixture? Chem. Mater. 27 (2015) 4459–4475.
[31] B.J. Sikora, C.E. Wilmer, M.L. Greenfield, R.Q. Snurr, Thermodynamic analysis of Xe/Kr selectivity in over 137000 hypothetical metal–organic frameworks, Chem. Sci. 3 (2012) 2217–2223.
[32] S.-J. Lee, S. Kim, E. Kim, M. Kim, Y.-S. Bae, Adsorptive separation of xenon/krypton mixtures using ligand controls in a zirconium-based metal-organic framework, Chem. Eng. J. 335 (2018) 345–351.
[33] X.Y. Chen, A.M. Plonka, D. Banerjee, R. Krishna, H.T. Schaef, S. Ghose, P. K. Thallapally, J.B. Parise, Direct Observation of Xe and Kr Adsorption in a Xe-selective microporous metal–organic framework, J. Am. Chem. Soc. 137 (2015) 7007–7010.
[34] T. Wang, Y.-L. Peng, E. Lin, Z. Niu, P. Li, S. Ma, P. Zhao, Y. Chen, P. Cheng, Z. Zhang, Robust bimetallic ultramicroporous metal–organic framework for separation and purification of noble gases, Inorg. Chem. 59 (2020) 4868–4873.
[35] Y.-P. Li, Y. Wang, Y.-Y. Xue, H.-P. Li, Q.-G. Zhai, S.-N. Li, Y.-C. Jiang, M.-C. Hu, X. Bu, Ultramicroporous building units as a path to Bi-microporous metal–organic frameworks with high acetylene storage and separation performance, Angew. Chem. Int. Ed. 58 (2019) 2–8.
[36] K.C. Stylianou, R. Heck, S.Y. Chong, J. Bacsa, J.T.A. Jones, Y.Z. Khimyak, D. Bradshaw, M.J. Rosseinsky, A Guest-responsive fluorescent 3D microporous metal−organic framework derived from a long-lifetime pyrene core, J. Am. Chem. Soc. 132 (2010) 4119–4130.
[37] K.C. Stylianou, J. Rabone, S.Y. Chong, R. Heck, J. Armstrong, P.V. Wiper, K. E. Jelfs, S. Zlatogorsky, J. Bacsa, A.G. McLen-nan, C.P. Ireland, Y.Z. Khimyak, K. M. Thomas, D. Bradshaw, M.J. Rosseinsky, Dimensionality transformation through paddlewheel reconfiguration in a flexible and porous Zn-based metal–organic framework, J. Am. Chem. Soc. 134 (2012) 20466–20478.
[38] J.E. Mondloch, W. Bury, D. Fairen-Jimenez, S. Kwon, E.J. De-Marco, M.H. Weston, A.A. Sarjeant, S.T. Nguyen, P.C. Stair, R.Q. Snurr, O.K. Farha, J.T. Hupp, Vapor-Phase metalation by atomic layer deposition in a metal–organic framework, J. Am. Chem. Soc. 135 (2013) 10294–10297.
[39] L.Y. Li, L.D. Guo, Z.G. Zhang, Q.W. Yang, Y.W. Yang, Z. B Bao, Q.L. Ren, J. Li, A robust squarate-based metal-organic framework demonstrates record high affinity and selectivity for Xenon over Krypton, J. Am. Chem. Soc. 141 (2019) 9358–9364.
[40] J. Liu, P. K Thallapally, D. Strachan, Metal-organic frameworks for removal of Xe and Kr from nuclear fuel reprocessing plants, Langmuir 28 (2012) 11584–11589.
[41] M.H. Mohamed, S.K. Elsaidi, T. Pham, K.A. Forrest, H.T. Schaef, A. Hogan, L. Wojtas, W. Xu, B. Space, M.J. Zaworotko, P.K. Thallapally, Hybrid ultra-microporous materials for selective xenon adsorption and separation, Angew. Chem. Int. Ed. 55 (2016) 8285–8489.
[42] Y.S. Bae, B.G. Hauser, Y.J. Colon, J.T. Hupp, O.K. Farha, R.Q. Snuee, High xenon/krypton selectivity in a metal-organic framework with small pores and strong adsorption sites, Microporous Mesoporous Mater. 169 (2013) 176–179.
[43] Y.L. Wang, W. Liu, Z. Bai, T. Zheng, M.A. Silver, Y. Li, Y. Wang, X. Wang, J. Diwu, Z. Chai, S. Wang, Employing a unique unsaturated Th4+ site in a porous thorium-organic framework for Kr/Xe uptake and separation, Angew. Chem. Int. Ed. 57 (2018) 5783–5787.
[44] K.B. Idrees, Z. Chen, X. Zhang, M.R. Mian, R.J. Drout, T. Islamoglu, O.K. Farha, Tailoring pore aperture and structural defects in zirconium-based metal–organic frameworks for krypton/xenon separation, Chem. Mater. 32 (2020) 3776–3782.

A robust metal-organic framework showing two distinct pores for effective separation of xenon and krypton

Li Wang[a], Jie Ding[a], Yudie Zhu[a], Zhenzhen Xu[a], Yaling Fan[a], Rajamani Krishna[b], and Feng Luo[*a]

[a] Jiangxi Key Laboratory for Mass Spectrometry and Instrumentation, School of Chemistry, Biology and Materials Science, East China University of Technology, Nanchang 330013, P. R. China

[b] Van‘t Hoff Institute for Molecular Sciences, University of Amsterdam, Science Park 904, 1098 XH Amsterdam, The Netherlands

E-mail: ecitluofeng@163.com

1. Experimental section

Materials and instrumentation

The H_4TBAPy was purchased from Jilin Chinese Academy of Sciences-Yanshen Technology Co.,Ltd. All other reagents and solvents were purchased from commercial sources without further purification.

The powder X-ray diffraction (PXRD) patterns were recorded on Bruker AXSD8 Discover powder diffractometer with Cu Kα, (λ= 1.5406 Å) at room temperature. The voltage and current were set at 40 kV, 40 mA. The data was collected in the range of 5-50 degree (2 theta). Thermal gravimetric analysis (TGA) was carried on TGA Q500 thermal analysis system at the temperature range from 30 to 800 °C under N_2 atmosphere. The heating rate was 10 °C/min. The data analysis was using the TA Universal Analysis software package.

X-ray Crystallography

X-ray diffraction data of **ECUT-51** was collected at 298 K on a Bruker-Appex (II) diffractometer using graphite monochromated MoKα radiation (λ=0.71073 Å). The data reduction included a correction for Lorentz and polarization effects, with an applied multi-scan absorption correction (SADABS). The crystal structure was solved and refined using the SHELXTL program suite. Direct methods yielded all non-hydrogen atoms, which were refined with anisotropic thermal parameters. All hydrogen atom positions were calculated geometrically and were riding on their respective atoms. The data can be obtained free of charge from the Cambridge Crystallographic Data Centre via www.ccdc.cam.ac.uk/data_ request/cif.

Grand Canonical Monte Carlo (GCMC) Simulations.

The GCMC simulations, which were performed by Sorption code in Material

Studio (MS) software, were carried out to investigate on the adsorbed capacity of MOF for Xe, Kr, and CO_2 at 298 K. A simulation box of 1×1×1 crystallographic unit cell was used. To guarantee the equilibration, 4×10^6 steps were performed. Rigid framework assumption was used in all simulations.

Density Functional Theory Calculations.

DFT calculations were performed to provide the optimized structures and energies of Xe, Kr, and CO_2 interaction with the framework of **ECUT-51**. The Perdew-Burke-Ernzerhof (PBE) function under the generalized gradient approximation (GGA) functional with the double-ξ numerical polarization (DPN) basis set was used by CASTEP program package in the Materiel Studio of Accelrys. The dispersion correction (DFT-D) was considered into calculations of the single point energy.

2. Gas adsorption calculations:

The isosteric heats of adsorption (Q_{st}) were calculated based on Clausius-Clapeyron equation and were calculated from the dual-site Langmuir-Freundlich model using

$$Q_{st} = RT^2\left(\frac{\partial \ln p}{\partial T}\right)_q \qquad (1)$$

Where p is the pressure, T is the temperature, R is the gas constant (8.314 J mol^{-1} K^{-1}). By drawing the lnP vs 1/T plot of gas at various loading, Q_{st} = -slope×R. To extract the converage-dependent isosteric heat of adsorption, the data were mo with a virial-type expression composed of parameters a_i and b_i that are independent of temperature.

The adsorption selectivity was established by the Ideal Adsorbed Solution Theory (IAST) for Xe/Kr (20:80), Xe/CO_2 (1:99), Xe/O_2 (1:99), and Xe/N_2 (1:99) mixtures at 298 K. The adsorption selectivity was calculated from

$$S_{ads} = \frac{q_A / q_B}{y_A / y_B} \quad (2)$$

where the q_A, and q_B represent the molar loadings in **ECUT-51** that is in equilibrium with a bulk fluid mixture with mole fractions y_A, and y_B = 1 - y_A. The molar loadings, also called *gravimetric uptake capacities*, are expressed in mol kg^{-1}.

3. Density Functional Theory Calculations:

The binding energy ΔE_{bind} for the adsorbed structures of the primitive cell with Xe/Kr/CO_2 was calculated by Eq. 3,

$$\Delta E_{bind} = E_{adsorbed} - E_{gas} - E_{MOF} \quad (3)$$

where, $E_{adsorbed}$, E_{gas}, and E_{MOF} are the total energies of adsorbed structure, single Xe, Kr or CO_2, and a unit cell of MOF.

Table S1. crystal data and structure refinements for **ECUT-51**

Compound	**ECUT-51**
Formula	$C_{22}H_{13}SrO_5$
Formula weight	444.94
Color	Light yellow
Crystal system	orthorhombic
Space group	*Pbam*
a(Å)	7.3372(6)
b(Å)	20.3580(16)
C (Å)	16.6199(12)
α	90.00
β	90.00
γ	90.00
Volume ($Å^3$)	2482.5
Z	4
Temperature for data collection (K)	296
Range for data collection θ(º)	2 to 25
No. of measured reflections	11989
No. of unique reflections	2274
No. of parameters	137
No. of restraints	14
Goodness-of-fit on F^2	1.097
Final R indexes[I≥2σ(I)]	R_1=0.0685, wR_2=0.2023
Final R indexes [all data]	R_1=0.0811, wR_2=0.2106

[a] $R_1 = \Sigma||F_o|-|F_c||/\Sigma|F_o|$. [b] $wR_2 = [\Sigma w (F_o^2-F_c^2)^2/\Sigma w (F_o^2)^2]^{1/2}$.

Table S2. Selected bond length (Å) and angles (°) for **ECUT-51**

Bond length			
Sr(1)-O(1)	2.473(4)	Sr(1) #1-O(3)	2.729(6)
Sr(1) #1-O(1)	2.645(4)	Sr(1)-O(1)#1	2.54037(6)
Sr(1) #1-O(2)	2.595(4)		

SymmetriSrl code: #1 -1/2+X,1/2-Y,-Z; #4 1/2+X,1/2-Y,-Z

Bond angles			
O(1)#1-Sr(1)-O(1)	77.2(2)	O(1)#2-Sr(1)-O(3)	132.45(12)
O(1)#1-Sr(1)-O(2)#2	154.11(16)	O(1)#3-Sr(1)-O(3)#3	84.02(16)
O(1)-Sr(1)-O(2)#2	86.23(19)	O(1)-Sr(1)-O(3)#3	84.02(16)
O(1)#1-Sr(1)-O(2)#3	86.23(19)	O(2)#2-Sr(1)-O(3)#3	114.20(14)
O(1)-Sr(1)-O(2)#3	154.11(16)	O(2)#3-Sr(1)-O(3)#3	114.20(14)
O(2)#2-Sr(1)-O(2)#3	101.4(3)	O(1)#2-Sr(1)-O(3)#3	68.90(14)
O(1)#1-Sr(1)-O(1)#2	152.92(9)	O(1)#3-Sr(1)-O(3)#3	68.90(14)
O(1)-Sr(1)-O(1)#2	99.36(17)	O(3)-Sr(1)-O(3)#3	150.1(2)
O(2)#2-Sr(1)-O(1)#2	49.05(14)	O(1)#3-Sr(1)-O(3)	132.45(12)
O(2)#3-Sr(1)-O(1)#2	104.29(18)	O(2)#3-Sr(1)-O(3)	83.41(14)
O(1)#1-Sr(1)-O(1)#3	99.36(17)	O(1)-Sr(1)-O(1)#3	152.92(9)
O(2)#2-Sr(1)-O(3)	83.41(14)	O(2)#3-Sr(1)-O(1)#3	49.05(14)
O(2)#2-Sr(1)-O(1)#3	104.29(18)	O(1)#2-Sr(1)-O(1)#3	71.4(2)
O(1)#1-Sr(1)-O(3)	72.81(15)	O(1)-Sr(1)-O(3)	72.81(15)

SymmetriSrl code: #1+X,+Y,-Z; #21/2+X,1/2-Y,+Z; #31/2+X,1/2-Y,-Z

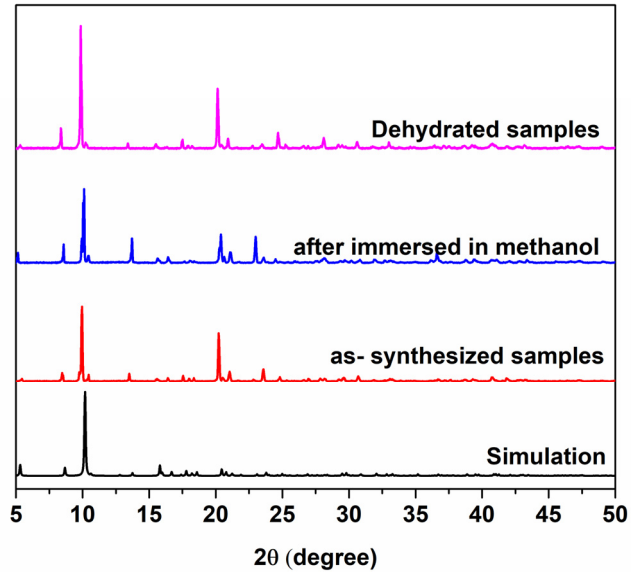

Fig. S1 PXRD patterns for **ECUT-51** after different treatments. The synthesized **ECUT-51** immersed into methanol 3 times per day for three days and then the PXRD pattern was collected. The immersed **ECUT-51** was heated at 100ºC under vacuum condition to obtain the dehydrated **ECUT-51**.

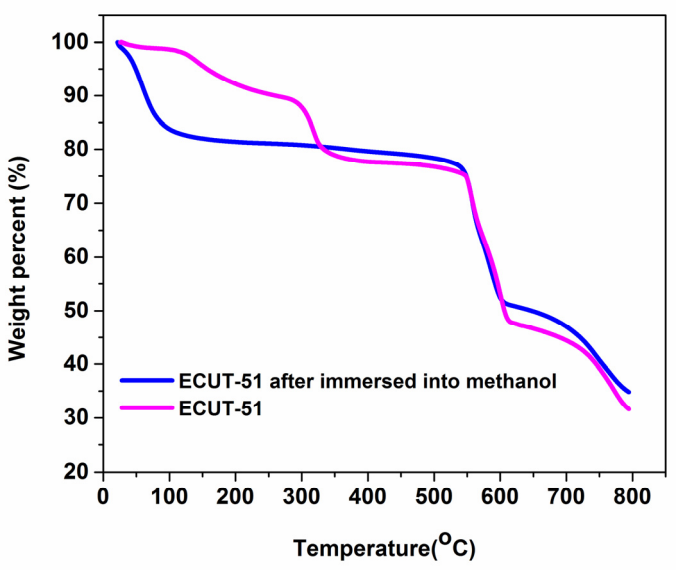

Fig. S2 The TGA curves of **ECUT-51** before and after immered into methanol from 25°C to 800°C under N_2 atmosphere.

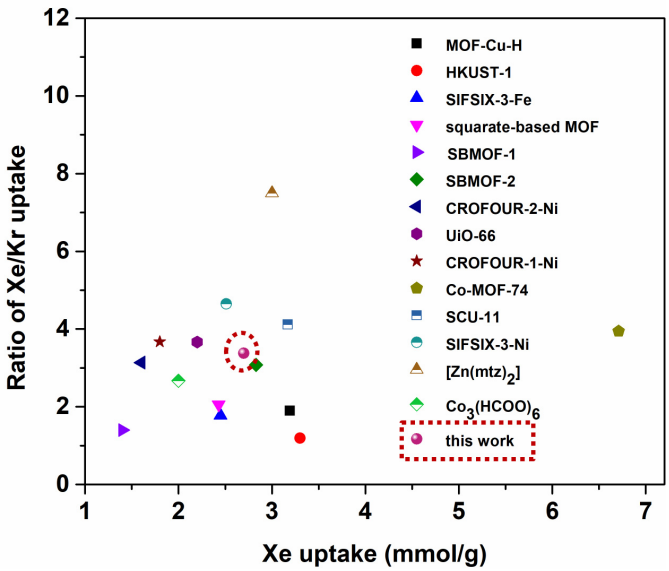

Fig. S3 A comparison of Xe/Kr uptake ratio at 298 K and 1 atm among our work and selected MOFs

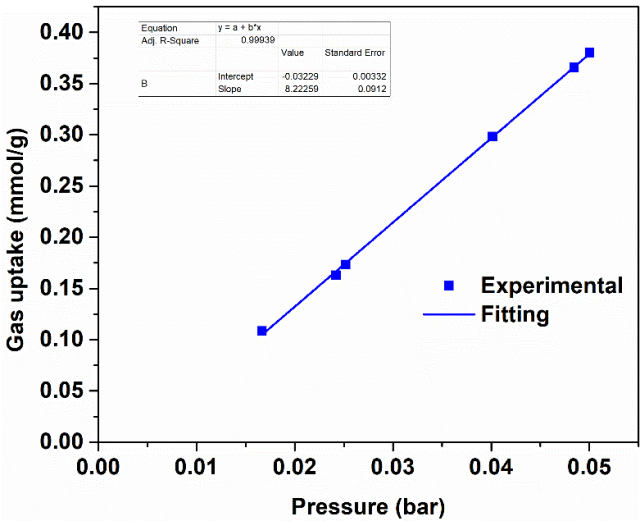

Fig. S4 The fitting of Xe adsorption isotherm in **ECUT-51**.

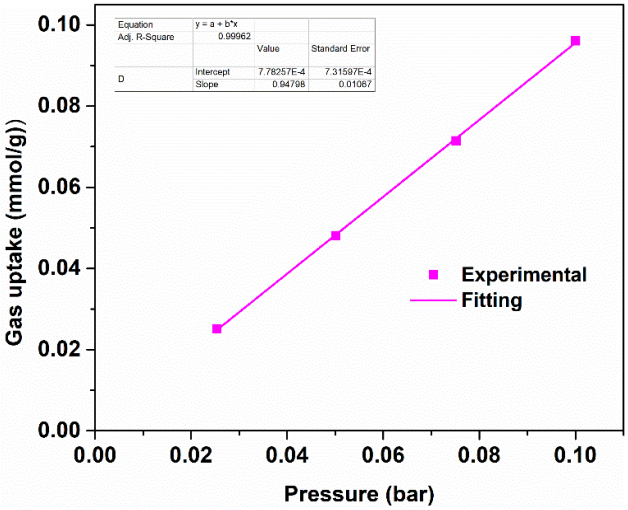

Fig.S5 The fitting of Kr adsorption isotherm in **ECUT-51**.

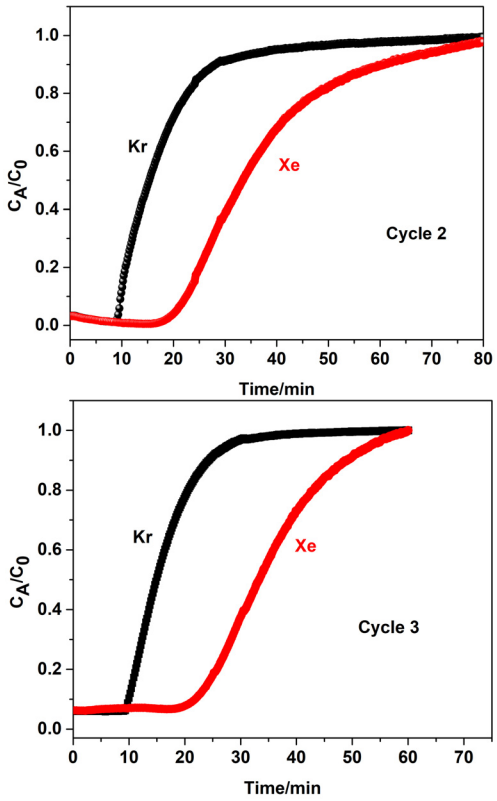

Fig. S6 Single column breakthrough experiments with Xe/Kr (20:80) using **ECUT-51a** for another 2 cycles.

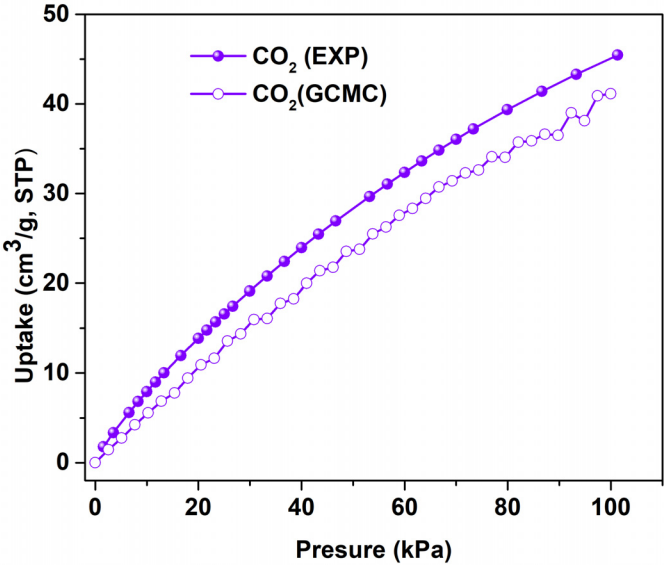

Fig. S7 The experimental and simulated adsorption isotherms of **ECUT-51** at 298K

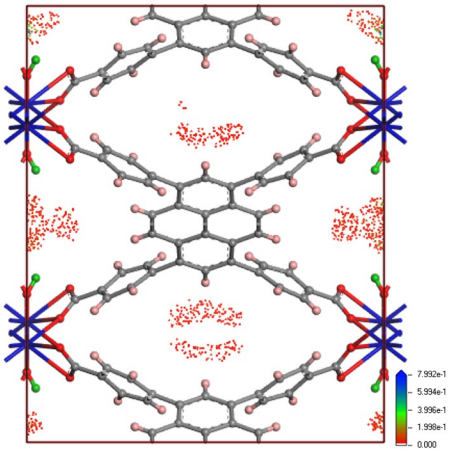

Fig. S8 Density distribution of CO_2 molecules in **ECUT-51** at 298 K and 100 kPa